# White Matter Microstructure Alterations in Early Psychosis and Schizophrenia

Tommaso Pavan[1], Yasser Alemán-Gómez[1], Raoul Jenni[2], Pascal Steullet[2], Zoé Schilliger[2,6], Daniella Dwir[2], Martine Cleusix[2], Luis Alameda[3,4,5], Kim Q. Do[2], Philippe Conus[3], Paul Klauser[2,6], Patric Hagmann[1] and Ileana Jelescu[1]

1. Department of Radiology, Lausanne University Hospital (CHUV) and University of Lausanne (UNIL)
2. Center for Psychiatric Neuroscience, Department of Psychiatry, Lausanne University Hospital and the University of Lausanne, Lausanne Switzerland
3. Service of General Psychiatry, Treatment and Early Intervention in Psychosis Program. Lausanne University Hospital (CHUV), Lausanne, Switzerland
4. Department of Psychosis Studies, Institute of Psychiatry, Psychology and Neuroscience. King's College of London, London, UK.
5. Centro Investigacion Biomedica en Red de Salud Mental (CIBERSAM); Instituto de Biomedicina de Sevilla (IBIS), Hospital Universitario Virgen del Rocio, Departamento de Psiquiatria, Universidad de Sevilla, Sevilla, Spain.
6. Service of Child and Adolescent Psychiatry, Department of Psychiatry, Lausanne University Hospital and the University of Lausanne, Lausanne, Switzerland

Corresponding author: Tommaso Pavan; address: *Centre de Recherche en Radiologie*, PET3, CHUV, Rue du Bugnon 46, 1011, Lausanne, Switzerland ; telephone:+41213146020; fax:+41213146020; email: tommaso.pavan@chuv.ch

# Abstract

Studies on schizophrenia feature diffusion magnetic resonance imaging (dMRI) to investigate white matter (WM) anomalies. The heterogeneity in the possible interpretations of typical Diffusion Tensor Imaging (DTI) metrics highlights the importance of increasing their specificity. Here, we characterize WM pathology in early psychosis (EP) and schizophrenia (SZ) with increased specificity using advanced dMRI: Diffusion Kurtosis Imaging and the biophysical model White Matter Tract Integrity – Watson (WMTI-W). This enables us to better characterize WM abnormalities and relate them to the patient's clinical characteristics and symptomatology. dMRI-derived microstructure features were extracted from all of WM and from individual tracts in 275 individuals. 93 subjects diagnosed with EP and 47 with SZ were compared respectively to 135 age-range matched healthy controls (HC). The relationships between the microstructure in WM and age at onset, aging trajectories, duration of illness, medication and various clinical scales were investigated in each patient group. WM diffusivities were higher, while kurtosis was lower in EP vs HC and in SZ vs HC. Differences were more pronounced in EP than SZ. WMTI-W model parameters suggest alterations to the extra-axonal compartment in EP and SZ as compared to HC. dMRI patterns in EP and SZ highly suggest WM deterioration in comparison to HC. The microstructure metrics involved point towards extra-axonal alterations, consistent with abnormal myelin integrity and WM deterioration. The direct link to symptomatology is however limited.

# Introduction

Psychosis is a psychiatric disorder with heavy implications for the affected individuals, their families, and society[1]. However, the disorder etiology remains only partially understood and considered multifactorial, involving a complex interplay of genetic, environmental, and neurobiological factors[2,3]. Many clinical studies investigating the psychosis spectrum[4–9] reported pathological white matter (WM) as a common feature of the disease. Most in vivo studies of WM abnormalities in psychosis use diffusion magnetic resonance imaging (dMRI), an MRI technique that relies on the random motion of water molecules to explore the cellular environment and thus infer the microstructural properties of the underlying biological tissue[10]. The most popular dMRI technique in clinical research is Diffusion Tensor Imaging (DTI) and its derived scalar metrics: fractional anisotropy (FA), mean/axial/radial diffusivities (MD/AD/RD). DTI is a so-called *signal representation*[11], which means it makes no assumption about the underlying tissue and reports on the apparent diffusivity in the voxel, in any given direction of space[12].

In schizophrenia (SZ) and early psychosis (EP), the most frequently reported and accepted dMRI patterns are reduced FA and increased MD[5,8,13–19], consistent with a loss of WM integrity and reduced diffusion barriers. Changes are widespread across the WM, with limited spatial consistency between studies[4,8,13,20]. Such heterogeneity may arise not only from cross-cohort heterogeneity[20] but also from different pathological processes affecting the WM, with some tracts showing non-degenerating early maturational shifts, or displaying accelerated aging[4]. Postmortem studies further substantiate the WM involvement found in first-episode psychosis participants[3] and in SZ, reporting splitting and decompacting of myelin sheaths together with dystrophic oligodendroglia[21–24] and microglia[25].

The heterogeneity in the possible DTI interpretations highlights the importance of improving the dMRI-derived microstructure characterization. A first step is to estimate the tissue diffusion properties more thoroughly, e.g. using Diffusion Kurtosis Imaging[26,27] (DKI), an extension of DTI that is estimated from stronger diffusion-weighting. DKI provides complementary information about tissue heterogeneity by going beyond the Gaussian DTI approximation and quantifying the variance of diffusivities across the voxel, arising from sub-domains such as cellular compartments. DKI has been able to detect widespread WM abnormality[28] in regions with complex fiber arrangement[29], subtle abnormalities in subjects at high risk for psychosis[30] and microstructural connectivity patterns associated to processing speed deficits in SZ[31].

Nevertheless, DTI and DKI metrics are only *sensitive* to features of the tissue microstructure and their changes can be the consequence of several possible pathological mechanisms (**Table 1)**. To gain specificity, WM *biophysical models* of diffusion are used[11], that capture the diffusion behavior in the underlying tissue with a mathematical model based on *a-priori* knowledge of the tissue structure. WM biophysical models often divide the voxel into two or more compartments, representing water inside and outside the axons, and sometimes the cerebrospinal fluid (CSF)[11,32]. Models previously used to characterize EP and SZ are free-water imaging[33] (FWI) and Neurite Orientation Dispersion and Density Imaging[34] (NODDI). Most FWI studies reported a global increase in free-water in SZ[35] and across lifespan[36]. NODDI detected decreased neurite density and increased orientation dispersion index in first-episode[37,38] and SZ[39]. However, both models display limitations in terms of *ad hoc* simplifying assumptions and fit constraints (e.g. in NODDI, all three compartment diffusivities are fixed[34,40]), strongly limiting the interpretability and validity[40] of the microstructure parameters estimated from the data[11,41].

In this work we use a more comprehensive biophysical model that overcomes these limitations. White Matter Tract Integrity-Watson[42,43] (WMTI-W, **Fig. 1**) enables the estimation of intra- and extra-axonal specific diffusivities that are excellent proxies for intra-axonal injury, inflammation and abnormal myelin integrity respectively[11,43,44], in addition to axonal density and orientation dispersion. WMTI and WMTI-W have been recently used to characterize WM pathology in a variety of pathological mechanisms (**Table 1**), patient populations[45] and animal models of disease[46,47], ranging from Alzheimer's disease[48–50] to traumatic brain injury[51], but, to our knowledge, never in schizophrenia.

Using WMTI-W, we aim to characterize for the first time WM pathology in EP and SZ with increased specificity, thus overcoming the inconsistencies previously found in EP and SZ literature and relate WM pathology to commonly used clinical measures and characteristics, such as age of psychosis onset, illness duration, medication, and symptomatology. In light of previous post-mortem ultrastructural findings of myelinated fiber pathology (myelin sheath splitting with inclusions of vacuoles, small-axons atrophy, dystrophic oligodendroglia[21–24]), we hypothesize that our dMRI findings will be mainly reflected as increased diffusivity of the extra-axonal space and as reduced axonal density.

# Methods

### Participants

The study was approved by the local Ethics Committee of the Canton of Vaud (CER-VD, Switzerland). Data were collected from 135 healthy controls (HC), 93 subjects with EP and 47 with SZ (**Table 2**). Participants with a diagnosis of EP (within 5 years after a first psychotic episode as defined by the CAARMS[52]) or SZ (DSM-IV diagnosis of

schizophrenia or schizoaffective disorder) were recruited from the Lausanne University Hospital. Exclusion criteria were psychosis related to intoxication, organic brain disease, IQ<70, alcoholism, drug abuse, major somatic disease, or current organic brain damage. Duration of illness, age at psychosis onset and medication were registered. HC were recruited from the same sociodemographic area of the clinical groups and were excluded if they had a first-degree family member who suffered from psychosis or prodromal symptoms, or if they reported current or past antipsychotic treatment. The HC group was further subdivided into younger (HC-Y, n=130, age=26.8±6.8) and older (HC-O, n=84, age=31.9±8.1) to better match the age ranges of the two clinical groups (EP=24.7±5.5; SZ=38.1±9.4 years). Within-group individual diagnoses are reported in **Supplementary Table S1.**

### MRI acquisition

MRI data were acquired on two different 3-Tesla systems (Magnetom TrioTim and PRISMA, Siemens Healthineers, Erlangen, Germany), each equipped with a 32-channel head coil. A 1-mm isotropic T1-weighted image was acquired for anatomical reference. Whole-brain diffusion-weighted images (DWI) were acquired using diffusion spectrum imaging (DSI) scheme across 15 b-values, ranging from 0 to 8000 s/mm$^2$, voxel size of 2.2 x 2.2 x 3 mm$^3$. Further information can be found in the 'Acquisition details' section of the Supplementary Material.

### Image preprocessing

The T1-weighted images were bias field corrected[53] and skull-stripped via nonlinear registration to the MNI-152 template using Advanced Normalization Tools[54] (ANTs). The diffusion preprocessing pipeline included MP-PCA denoising, Gibbs ringing-, EPI-, eddy current and motion corrections, following most recent guidelines[55] - see Supplementary Material for preprocessing details.

### Microstructure estimation

For DKI and WMTI-W estimation, the diffusion dataset was truncated at b≤2500 s/mm$^2$ (Jensen et al., 2005). DKI was fit voxel-wise[56] using Matlab, from which seven parameter maps were derived. Four from DTI: RD, MD, AD and FA, and three from DKI: radial, mean, axial kurtosis (RK, MK, AK). Then, WMTI-W model parameters were estimated voxel-wise from the DTI and DKI parameters, using an in-house Python script, yielding other five parameter maps: axonal density $f$, intra-axonal diffusivity $D_a$, extra-axonal parallel and perpendicular diffusivities $D_{e,||}$, $D_{e,\perp}$ and axon orientation alignment $c_2$ (**Fig. 1**). The WM characterization thus relied on 12 microstructure metrics.

### ROI analysis

Individual FA maps were non-linearly registered to the Johns Hopkins University FA template[57] (JHU) using ANTs, and the WM region-of-interest (ROI) atlas labels were mapped back to individual space . WM ROI definition using the atlas approach was preferred to subject-specific tractography-based reconstruction because it allows easier and more direct comparison with the large body of literature also using the JHU WM atlas. The mean value of each microstructure metric was computed for each ROI, as well as in the whole-WM mask defined as the collection of all JHU ROIs (from here on referred to as 'WM core').

### Psychiatric scales

Psychiatric tests included the Global Assessment of Functioning[58] scale (GAF), the Positive and Negative Syndrome Scale[59] (PANSS), and the Montgomery-Asberg Depression Rating Scale[60] (MADRS). For the PANSS, items were categorized using the Wallwork/Fortgang five-factor model[61]. PANSS data was not available for 5 EP and 1 SZ subjects, MADRS was not assessed in 6 EP and 16 SZ subjects.

### Statistical analysis

Before any statistical analysis, all the microstructure parameter estimates in the WM core and individual JHU ROIs were harmonized for scanner type via ComBat harmonization[62] that was proven efficient at correcting scanner effects in the same cohort[63]. Distributions for each metric, ROI and group were tested for normality using the Shapiro–Wilk test and for homogeneity of variance using the Levene's Test. The statistical test used for group comparisons was chosen based on distribution characteristics, resulting in microstructure metrics for the WM core being tested via non-parametric *Wilcoxon* signed-rank test, suitable for non-normal but homogeneous variance distributions. At the ROI level, microstructure metrics between groups were compared using the non-parametric *Brunner-Munzel*[64,65] test, suitable for distributions with unequal variances. In all comparisons, the estimates were controlled for sex and quadratic age (the model selection procedure for the age correction is detailed in the Supplementary Material). False-Discovery Rate (FDR) correction was applied to control for false positives. In total, 24 tests (12 metrics × 2 group pairs) were conducted for group differences between metrics in the WM core, and 1200 tests for ROI-specific group

differences (12 metrics × 50 JHU ROIs × 2 group pairs). Effect sizes ($r$) for each comparison were estimated according to the type of test (*Wilcoxon*: $r_w$, *Brunner-Munzel*: $r_{bm}$), see Supplementary Materials for details. The dice coefficient was used to quantify the similarity in ROI alterations across the brain, indicating the proportion (between 0 and 1) of significant alterations that EP and SZ groups have in common.

Associations of the microstructure with clinical characteristics: slope contrasts between the various metrics in the WM core and age at first psychosis, duration of illness, and chlorpromazine-equivalent dose (CPZ-equivalent) were estimated in R[66]. Each regression was corrected for quadratic age and sex, and p-values were FDR corrected. Between-group differences in aging trajectories for the microstructure metrics were estimated in a similar manner, but this time pooling HC vs clinical participants (EP + SZ) and correcting only for sex and FDR.

Associations of the microstructure metrics with psychiatric scales: participants with a delay between clinical assessment and MRI scan larger than 45 days were excluded from this analysis to ensure good temporal correspondence between psychiatric status and brain microstructure. The exclusion left 58 EP (mean delay .43±.6 months) and 33 SZ (.58±.42 months) available for the analysis. The correlation matrices between WM core metrics and psychiatric scales for EP and SZ were analyzed via hierarchical clustering in R[66] with the objective of clustering similar relationships between symptoms and WM microstructure. Correlation p-values were FDR-corrected (12 metrics × 8 dimensions × 2 groups = 192 tests).

# Results

### Demographics

**Table 2** collects cohort demographics. Age was significantly different between clinical participants and controls (i.e., EP vs HC-Y, p=0.03) and SZ vs HC-O, p<.0001). Illness duration was longer in SZ than in EP group (p<.0001).

### Microstructure imaging estimates in the white matter cores

Study templates for DTI, DKI and WMTI-W metrics are plotted in **Fig. S2**. The harmonized mean estimates of the WM core for the four groups are reported in **Table S2**. In the WM core, several group differences were found (**Fig. 2**).

Compared to HC-Y, EP showed significantly higher DTI diffusivities and lower FA (**Fig. 2A-D**; RD, MD, FA: p<.0001, AD: p=.014), as well as lower kurtosis (**Fig. 2E-G**; RK: p=.0017, MK: p=.0029; AK: p=.035). Axonal water fraction, $f$, and alignment, $c_2$, in EP were also significantly lower than in HC-Y (**Fig. 2H, L**; $f$: p=.0053 $c_2$: p=.0010), while extra-axonal diffusivities, $D_{e,//}$ and $D_{e,\perp}$, were higher (**Fig. 2J, K**; $D_{e,//}$: p=.0010, $D_{e,\perp}$: p<.0001). No significant differences were found between EP and HC-Y in terms of intra-axonal diffusivity $D_a$ (**Fig. 2I**). Effect sizes were low to medium with the highest being RD ($r_w$=.32), followed by MD ($r_w$=.31), $D_{e,\perp}$ ($r_w$=.30), and FA ($r_w$=.29).

Differences between SZ and HC-O were more limited, with no significant DTI metric. Kurtosis, however, was lower in SZ (**Fig. 2E-G**; RK: p=.035, MK: p=.020, AK: p=.035) with a small effect size (average $r_w$=.20). The WMTI-W model revealed reduced $f$ (**Fig. 2H**; p=.035), increased $D_a$ (**Fig. 2I**; p=.017), and $D_{e,||}$ (**Fig. 2J**, p=.035). $D_{e,||}$ and $D_a$ showed the largest effect size ($r_w$=.24 and .23). A complete list of p-values, effect sizes and confidence intervals are found in **Table S3**. We found no significant differences between EP and SZ (**Table S4**).

### Microstructure imaging estimates of the white matter tracts

Group comparison of the JHU ROIs revealed distinct patterns in the microstructure metrics tendencies, highlighting ROI specific alterations in both EP and SZ (**Fig. 3**). Bundles showing the strongest group differences included the corpus callosum (CC), fornix (FX), corona radiata (CR), posterior thalamic radiation (PTR), sagittal stratum (SAGSTR), cingulum (CING/CG) and superior longitudinal fasciculus (SLF). Common features were higher DTI diffusivities in both EP and SZ with respect to their HC groups, with the EP group having the most distinct and widespread increase across the WM. The percentages of WM ROIs with higher RD, MD, and AD were: 56, 54, 18% in EP and 12, 16, 8% in SZ. These differences were generally paired to lower FA of the same ROIs in EP, but not as consistently in SZ (34 vs 4%).

Kurtosis metrics were lower in both patient groups. In EP, the significantly lower DKI metrics were matched to the increase in DTI metrics except for the bilateral cerebellar peduncle (CP) and CING (hippocampal section acc. JHU) areas. Decreased kurtosis was significant for RK, MK and AK in 24%, 34% and 20% of ROIs, respectively. In SZ, this trend was notably less consistent (RK: 20%, MK: 24%, AK: 12% of ROIs), with some ROIs showing alterations detected by DKI and not DTI, such as the bilateral SAGSTR, the left anterior limb of internal capsule (ALIC) and FX and vice versa, e.g. in CING and right anterior corona radiata (ACR).

WMTI-W metrics displayed the same trends as for the whole WM analysis, with $f$ lower in several locations of the WM in SZ and especially EP (10% vs 18% of ROIs), and higher extra-axonal diffusivities. In EP, $D_{e,//}$ and $D_{e,\perp}$ were significantly altered in 24 and 20% of the ROIs respectively. In the SZ group, $D_{e,//}$ and $D_{e,\perp}$ showed fewer number of

significant alterations, 16% and 6%. Notably, $D_a$ alterations were uncommon in both groups and not spatially consistent. Finally, sparse $c_2$ alterations were found in EP (6% of ROIs) but none in SZ .

Overall, the Dice coefficient between EP and SZ differences to their respective HC revealed 36% of EP and SZ ROI alterations to be common to both groups. The effects sizes for both groups compared to their HC were on average medium (mean EP $r_{bm}$=.48, SZ $r_{bm}$=.50), with highest effect size found in the FA of the left CP in EP ($r_{bm}$=.68) and the AK of the left SCR in SZ ($r_{bm}$=.75). Kurtosis metrics and FA showed the strongest effect sizes on average across the metrics and ROIs ($r_{bm}$≈.55). $f$ showed the highest average effect size among the WMTI-W metrics ($r_{bm}$=.54). For additional details about FDR p-values, effect sizes and confidence intervals see **Table S5** and **Table S6**.

### Association between microstructure estimates and clinical characteristics

We correlated the clinical characteristics to the WM core microstructure (i.e., averaged measure across all WM tracts) because the microstructure metrics showed widespread consistent changes across JHU ROIs in patients. Furthermore, this approach limits considerably the number of statistical tests. There were no significant associations between WM microstructure and age at psychosis onset (**Fig. S3**), nor with illness duration (**Fig. S4**). The intra-axonal diffusivity, $D_a$, showed significant negative association with CPZ-equivalent dose in the SZ group (p=.013), which was significantly different from EP (p=.0019, **Fig. S5I**). Notably, $D_{e,//}$, showed similar yet non-significant trends to $D_a$. Finally, to better understand the aging trajectories of WM microstructure in patients vs. HC we examined the interaction between age and the two grouping variables (EP+SZ) and HC. No significant differences were found after FDR correction (12 tests). Individual age trajectories for each dMRI metric can be found in **Fig. S6**.

### Association between microstructure estimates and psychopathological symptom domains

We examined associations between microstructure metrics in the WM core and symptom scores . Differences in psychiatric scales between EP and SZ, and the average delay between psychiatric evaluation and MRI scan for the whole cohort are reported in **Table 2**.

Overall, correlations between psychiatric scales and WM microstructure metrics were stronger in SZ than EP (**Fig. 4B** vs **A**). However, no correlation survived FDR correction (192 tests). In EP, hierarchical clustering identified two macro clusters of microstructure metrics (**Fig. 4A** top dendrograms, clustering of columns): i) diffusivities cluster (RD, MD, AD, $D_{e,//}$, $D_{e,\perp}$, $D_a$) and ii) kurtosis and anisotropy cluster (RK, AK, MK, $f$, FA, $c_2$), informing about the tissue complexity. Contrary to the trends of dMRI group differences between EP vs HC-Y (higher diffusivities and lower kurtosis in the patient vs HC group), GAF score correlated positively with the diffusivities cluster (i) and negatively with the kurtosis cluster (ii). Thus, higher functioning corresponded to faster diffusivities and to lower FA, kurtosis and $f$. Scores for all the psychiatric dimensions also revealed decreased diffusivities and increased kurtosis with worsening of the symptoms (**Fig. 4A**).

In SZ, similar clusters were found for i) diffusivities (RD, MD, AD, $D_{e,//}$, $D_{e,\perp}$), however $D_a$ was clustered with the ii) kurtosis and anisotropy cluster (RK, AK, MK, $f$, FA, $c_2$, $D_a$, **Fig. 4B**, vertical clustering). The clustering of the symptom dimensions differed from EP. The GAF showed positive correlation with the kurtosis and anisotropy metrics cluster (ii), while negative correlation with the diffusivities cluster (i), consistent with trends in dMRI group differences of elevated diffusivities and reduced kurtosis in SZ vs HC-O. Similarly, PANSS exc. scores correlated with increased diffusivities (i), and decreased complexity (ii, **Fig. 4B**, first horizontal cluster), although these effects should be treated with caution, given the low scores and the absence of acute manic states in the cohort. Finally, a second cluster comprising the rest of the PANSS scales and the MADRS mainly showed consistent negative correlations with $D_a$ and $c_2$. Although we underline that none of these associations was significant after FDR, the consistency of positive and negative associations across the scores and cluster blocks suggests they may not be random.

# Discussion

With the present analysis we employed more advanced diffusion metrics than DTI, namely DKI and a comprehensive microstructure model, WMTI-W, both aimed at characterizing the WM pathology with increased sensitivity and specificity in EP and SZ cohorts.

Our findings reveal that WM alterations are already present and widespread in the EP stage and differences in microstructure are in fact less pronounced between chronic SZ and HC-O when accounting for age. Such results support the developmental interpretation of schizophrenia according to which systematic FA differences to HC originate during adolescence and remain through the lifespan[67–70]. In this context, the widespread alterations found in EP could result from a shift in peaks in the WM development, achieved earlier in patients[4,69] than HC. In other words, for a similar age, WM in EP could already have peaked and be on the decline while the HC-Y is still maturing. Consequently, the less widespread differences in SZ vs HC-O could be attributed to the WM maturational shift rather than accelerated aging[69] for which stronger and more widespread alterations are expected. However, the less

pronounced alterations in SZ can also be explained by the SZ cohort size with respect to the wide age range, which could cause the underestimation of the alterations from a statistical perspective. Supporting this last conclusion are the age-trajectories of our cohort that did not significantly differ between EP and SZ participants when compared to HC, while differences in age trajectories between the two stages of the disease are often reported[4,69,71].

In accordance with our hypothesis, most EP and SZ WM differences to HC concerned the radial direction of diffusion, i.e., perpendicularly to the bundle main axis. Thus, RD and MD were the most affected, while AD differences were less significant. Our study confirms previous DTI[4,17,67], dMRI microstructure[63,72] and post-mortem cytoarchitectural[3] alterations found already at the EP stage, and the widespread reduced FA and increased MD[4–6,13–15,17,19,38,67,73], RD and AD[6,16,74,75] in areas commonly reported in both EP and chronic SZ.

In addition, WM kurtosis was lower for both patient groups, but also more pronounced in EP, and more particularly in the radial direction with a moderate effect size, representing a decrease in tissue complexity and heterogeneity[26,27,44]. Remarkably, in SZ vs HC-O, DKI was able to identify differences in WM ROIs (SAGSTR, left ALIC and FX) that were not evident in DTI. In a review from Pasternak et al.[76], all studies but one also reported reduced MK, with one study also reporting lower RK and AK in SZ[29].

Our ROI-specific differences in microstructure metrics between EP or SZ participants and controls were consistent with literature, as previous studies also reported alterations in CING[4], FX[77,78], CR[79–81], PTR[81,82] and SAGSTR[82] in EP, that remained present in SZ. CC and SLF[4,15] are considered to have a declining trajectory with aging in SZ[4,15] (either FA decrease or MD increase when compared to HC), but our results confirm only the SLF trajectory (increased MD, decreased FA in EP and decreased kurtosis in SZ), while the CC was not altered as much in SZ as in EP[4,77–82].

For the first time, we used WMTI-W, a comprehensive biophysical model of WM, to tease apart possible pathological contributions to the reported WM differences. In EP, WMTI-W helps attribute the observed alterations to the extra-axonal compartment, due to the significant increase in $D_{e,//}$ and $D_{e,\perp}$, but not $D_a$. The lower axonal water fraction $f$ and orientation coherence $c_2$ are further consistent with pathological features such as altered myelination and axonal density. The former have indeed been shown to induce an increase in $D_{e,\perp}$ and decrease in $f$[46,47] (**Table 1**) while the increase in $D_{e,//}$ can be a consequence of overall reduced cellular density and thereby hindrance in the extra-axonal space. The SZ group was overall characterized by higher $D_{e,//}$ and lower $f$, also pointing to less densely packed extra-cellular space. The WM core analysis suggested also higher intra-axonal diffusivity $D_a$ in this group, but only two specific ROIs sustained this trend (CING and CC). Previous works using NODDI[34], a comparable but more constrained biophysical model, also reported reduced neurite density (comparable to $f$) in several ROIs and increased orientation dispersion index (corresponding to lower $c_2$) in both first episode and chronic SZ[72]. These patterns of preferentially altered extra-axonal environment are also consistent with reports of global increase in "free water" using the FWI technique in SZ cohorts[35], although FWI conflates potential pathological mechanisms by defining a tissue compartment (intra- and extra-axonal) vs a free water (CSF) one.

The pathological WM changes suggested by WMTI-W are indeed supported by neuroimaging findings beyond dMRI, such as a 14% reduction in WM volume[83], and ultrastructural post-mortem studies reporting myelinated WM fiber pathology, such as decompacting and splitting of the myelin sheath, inclusions of vacuoles in-between myelin layers, small-axons atrophy, and the presence of swollen or dystrophic oligodendroglia[22–24] and microglia[25]. In parallel to these morphological changes, a 27-28% reduction in oligodendrocyte densities were reported in cortical layer III and subcortical areas[21] of SZ specimens.

The lack of significant associations of WM microstructure metrics with age at first psychosis, medication or with the duration of illness is aligned with the literature[84]. The correlations between WM microstructure and symptoms were also weak and non-significant, despite in accordance with previous studies[8]. Speculatively, this scenario could be caused by competing pathological mechanisms between deterioration[4]-abnormal myelination[46] vs neuroinflammation[44] (demyelination vs microgliosis-astrogliosis in **Table 1**) that have opposite effects on microstructure metrics and, when combined, result in a challenging interpretation. Indeed, neuroinflammation has the effect of reducing diffusivities and increasing kurtosis due to higher cellular crowding associated with microgliosis and astrocytosis[44,46,47,85]. In support of this mechanism, proinflammatory cytokines have been reported to be elevated in EP[86] and SZ[87], and were related to negative symptoms in EP[86]. Furthermore, this interpretation would explain the unconvincing/absence of associations between symptoms and microstructure metrics often reported[8].

Supported by previous postmortem ultrastructural findings, our results point in the direction of pathological myelination and we foresee a motivation to use advanced dMRI for tracking disease progression of this aspect of the pathology, and possibly distinguish myelin loss from axonal loss[47] or atrophy. However, given the small to medium effect sizes found in most of the microstructure metrics (**Table S3, 5, 6**), their applicability may be limited to group level studies and not at individual level if not assessed in the context of a reference norm (e.g. normative modelling[88]).

Several questions also remain open with regards to the evolution of the pathology and how changes to the diffusion metrics behave during acute psychosis phases. Going forward, dMRI combined with careful biophysical modeling could continue to provide crucial information about cellular-level brain changes in EP and SZ in vivo and longitudinally.

The first two main limitations of the present study are the use of the age-range approach instead of age-matching and the use of data from two scanners that is a source of bias, possibly even after careful harmonization. The age-range approach was preferred to maintain the sample size as large as possible to better correct for the scanner effect and increase the statistical power of the analyses. In addition, we believe it was preferable not to pair participants by age at the cost of pairing data from different scanners, which could introduce more bias. With regards to the WM biophysical model, the modeling of the axonal dispersion as Watson distribution is not ideally suited for multi-fiber configurations, e.g. crossing fibers[11]. Furthermore, as symptoms are transitory in nature, the patient's symptomatic state at the time of the MRI scan may differ from the state that led to the assigned clinical score. This mismatch highlights the challenges of relating brain pathology characterized non-invasively using dMRI to symptomatology and the necessity to embrace different approaches to face such heterogeneity (e.g. normative modelling[20]). In the light of the limitations of the present study, the generalizability of our conclusions needs to be confirmed in other cohorts.
In conclusion, with this work we demonstrated that WM alterations, already present at the early psychosis stages, manifest preferentially perpendicular to the axons as major extra-cellular increase in diffusivities, decreased intra-cellular water fraction, and loss of fiber alignment, consistent with early myelin aberrations and shifted maturation. Remarkably, with time, these differences become less dramatic in chronic SZ as compared to age range-matched controls.

# Acknowledgments

This work was supported by the Swiss National Science Foundation (PCEFP2_194260, to I.J.), the National Center of Competence in Research (NCCR) "SYNAPSY - The Synaptic Bases of Mental Diseases" from the Swiss National Science Foundation (n° 51NF40 – 185897 to KQD & PC) and the Foundation Alamaya. LA is supported by Carigest fellowship. PK, DD and LA are supported by the Adrian & Simone Frutiger Foundation .

# Conflict of Interest

The authors have nothing to disclose and there are no conflicts of interest.

# References

1. Wittchen, H. U. *et al.* The size and burden of mental disorders and other disorders of the brain in Europe 2010. *Eur. Neuropsychopharmacol. J. Eur. Coll. Neuropsychopharmacol.* **21**, 655–679 (2011).
2. Keshavan, M. S. *et al.* Neurobiology of early psychosis. *Br. J. Psychiatry* **187**, s8–s18 (2005).
3. Harrison, P. J. The neuropathology of schizophrenia: A critical review of the data and their interpretation. *Brain* **122**, 593–624 (1999).
4. Cetin-Karayumak, S. *et al.* White matter abnormalities across the lifespan of schizophrenia: a harmonized multi-site diffusion MRI study. *Mol. Psychiatry* **25**, 3208–3219 (2020).
5. Friedman, Joseph I. *et al.* Diffusion Tensor Imaging Findings in First-Episode and Chronic Schizophrenia Patients. *Am. J. Psychiatry* **165**, 1024–1032 (2008).
6. Barth, C. *et al.* In vivo white matter microstructure in adolescents with early-onset psychosis: a multi-site mega-analysis. *Mol. Psychiatry* **28**, 1159–1169 (2023).
7. Karlsgodt, K. H. White Matter Microstructure across the Psychosis Spectrum. *Trends Neurosci.* **43**, 406–416 (2020).
8. Kelly, S. *et al.* Widespread white matter microstructural differences in schizophrenia across 4322 individuals: results from the ENIGMA Schizophrenia DTI Working Group. *Mol. Psychiatry* **23**, 1261–1269 (2018).

9. van Velzen, L. S. *et al.* White matter disturbances in major depressive disorder: a coordinated analysis across 20 international cohorts in the ENIGMA MDD working group. *Mol. Psychiatry* **25**, 1511–1525 (2020).
10. Beaulieu, C. The basis of anisotropic water diffusion in the nervous system - a technical review. *NMR Biomed.* **15**, 435–455 (2002).
11. Jelescu, I. O. & Budde, M. D. Design and Validation of Diffusion MRI Models of White Matter. *Front. Phys.* **5**, (2017).
12. Le Bihan, D. *et al.* Diffusion tensor imaging: Concepts and applications. *J. Magn. Reson. Imaging* **13**, 534–546 (2001).
13. Dwork, A. J., Mancevski, B. & Rosoklija, G. White matter and cognitive function in schizophrenia. *Int. J. Neuropsychopharmacol.* **10**, 513 (2007).
14. Pasternak, O., Westin, C.-F., Dahlben, B., Bouix, S. & Kubicki, M. The extent of diffusion MRI markers of neuroinflammation and white matter deterioration in chronic schizophrenia. *Schizophr. Res.* **161**, 113–118 (2015).
15. Waszczuk, K. *et al.* Relationship between White Matter Alterations and Pathophysiological Symptoms in Patients with Ultra-High Risk of Psychosis, First-Episode, and Chronic Schizophrenia. *Brain Sci.* **12**, 354 (2022).
16. Klauser, P. *et al.* White Matter Disruptions in Schizophrenia Are Spatially Widespread and Topologically Converge on Brain Network Hubs. *Schizophr. Bull.* **43**, 425–435 (2017).
17. Tamnes, C. K. & Agartz, I. White Matter Microstructure in Early-Onset Schizophrenia: A Systematic Review of Diffusion Tensor Imaging Studies. *J. Am. Acad. Child Adolesc. Psychiatry* **55**, 269–279 (2016).
18. Kraguljac, N. V. *et al.* Neuroimaging Biomarkers in Schizophrenia. *Am. J. Psychiatry* **178**, 509–521 (2021).
19. Sagarwala, R. & Nasrallah, H. A. The effect of antipsychotic medications on white matter integrity in first-episode drug-naïve patients with psychosis: A review of DTI studies. *Asian J. Psychiatry* **61**, 102688 (2021).
20. Lv, J. *et al.* Individual deviations from normative models of brain structure in a large cross-sectional schizophrenia cohort. *Mol. Psychiatry* **26**, 3512–3523 (2021).
21. Hof, P. R. *et al.* Loss and altered spatial distribution of oligodendrocytes in the superior frontal gyrus in schizophrenia. *Biol. Psychiatry* **53**, 1075–1085 (2003).
22. Uranova, N. A., Vikhreva, O. V., Rachmanova, V. I. & Orlovskaya, D. D. Ultrastructural Alterations of Myelinated Fibers and Oligodendrocytes in the Prefrontal Cortex in Schizophrenia: A Postmortem Morphometric Study. *Schizophr. Res. Treat.* **2011**, e325789 (2011).

23. Uranova, N. A., Vikhreva, O. V., Rakhmanova, V. I. & Orlovskaya, D. D. Ultrastructural pathology of oligodendrocytes adjacent to microglia in prefrontal white matter in schizophrenia. *Npj Schizophr.* **4**, 1–10 (2018).
24. *The Neuropathology of Schizophrenia*. (Springer International Publishing, Cham, 2021). doi:10.1007/978-3-030-68308-5.
25. Uranova, N. A., Vikhreva, O. V., Rakhmanova, V. I. & Orlovskaya, D. D. Dystrophy of Oligodendrocytes and Adjacent Microglia in Prefrontal Gray Matter in Schizophrenia. *Front. Psychiatry* **11**, (2020).
26. Jensen, J. H., Helpern, J. A., Ramani, A., Lu, H. & Kaczynski, K. Diffusional kurtosis imaging: The quantification of non-gaussian water diffusion by means of magnetic resonance imaging. *Magn. Reson. Med.* **53**, 1432–1440 (2005).
27. Jensen, J. H. & Helpern, J. A. MRI quantification of non-Gaussian water diffusion by kurtosis analysis. *NMR Biomed.* **23**, 698–710 (2010).
28. Narita, H. *et al.* Mean kurtosis alterations of cerebral white matter in patients with schizophrenia revealed by diffusion kurtosis imaging. *Prog. Neuropsychopharmacol. Biol. Psychiatry* **71**, 169–175 (2016).
29. Zhu, J. *et al.* Performances of diffusion kurtosis imaging and diffusion tensor imaging in detecting white matter abnormality in schizophrenia. *NeuroImage Clin.* **7**, 170–176 (2015).
30. Zhang, F. *et al.* MK-Curve improves sensitivity to identify white matter alterations in clinical high risk for psychosis. *NeuroImage* **226**, 117564 (2021).
31. Kochunov, P. *et al.* Diffusion-weighted imaging uncovers likely sources of processing-speed deficits in schizophrenia. *Proc. Natl. Acad. Sci.* **113**, 13504–13509 (2016).
32. Novikov, D. S., Fieremans, E., Jespersen, S. N. & Kiselev, V. G. Quantifying brain microstructure with diffusion MRI: Theory and parameter estimation. *NMR Biomed.* **32**, e3998 (2019).
33. Pasternak, O., Sochen, N., Gur, Y., Intrator, N. & Assaf, Y. Free water elimination and mapping from diffusion MRI. *Magn. Reson. Med.* **62**, 717–730 (2009).
34. Zhang, H., Schneider, T., Wheeler-Kingshott, C. A. & Alexander, D. C. NODDI: practical in vivo neurite orientation dispersion and density imaging of the human brain. *NeuroImage* **61**, 1000–1016 (2012).
35. Carreira Figueiredo, I., Borgan, F., Pasternak, O., Turkheimer, F. E. & Howes, O. D. White-matter free-water diffusion MRI in schizophrenia: a systematic review and meta-analysis. *Neuropsychopharmacology* **47**, 1413–1420 (2022).

36. Cetin-Karayumak, S. *et al.* Characterization of the extracellular free water signal in schizophrenia using multi-site diffusion MRI harmonization. *Mol. Psychiatry* 1–9 (2023) doi:10.1038/s41380-023-02068-1.
37. Rae, C. L. *et al.* Deficits in Neurite Density Underlie White Matter Structure Abnormalities in First-Episode Psychosis. *Biol. Psychiatry* **82**, 716–725 (2017).
38. Kraguljac, N. V. *et al.* White matter integrity, duration of untreated psychosis, and antipsychotic treatment response in medication-naïve first-episode psychosis patients. *Mol. Psychiatry* **26**, 5347–5356 (2021).
39. Kraguljac, N. V. *et al.* A longitudinal neurite and free water imaging study in patients with a schizophrenia spectrum disorder. *Neuropsychopharmacology* **44**, 1932–1939 (2019).
40. Novikov, D. S., Kiselev, V. G. & Jespersen, S. N. On modeling. *Magn. Reson. Med.* **79**, 3172–3193 (2018).
41. Jelescu, I. O., Veraart, J., Fieremans, E. & Novikov, D. S. Degeneracy in model parameter estimation for multi-compartmental diffusion in neuronal tissue. *NMR Biomed.* **29**, 33–47 (2016).
42. Jespersen, S. N., Olesen, J. L., Hansen, B. & Shemesh, N. Diffusion time dependence of microstructural parameters in fixed spinal cord. *NeuroImage* **182**, 329–342 (2018).
43. Fieremans, E., Jensen, J. H. & Helpern, J. A. White matter characterization with diffusional kurtosis imaging. *NeuroImage* **58**, 177–188 (2011).
44. Jelescu, I. O. & Fieremans, E. Chapter 2 - Sensitivity and specificity of diffusion MRI to neuroinflammatory processes. in *Advances in Magnetic Resonance Technology and Applications* (eds. Laule, C. & Port, J. D.) vol. 9 31–50 (Academic Press, 2023).
45. Kamiya, K. *et al.* Diffusion imaging of reversible and irreversible microstructural changes within the corticospinal tract in idiopathic normal pressure hydrocephalus. *NeuroImage Clin.* **14**, 663–671 (2017).
46. Guglielmetti, C. *et al.* Diffusion kurtosis imaging probes cortical alterations and white matter pathology following cuprizone induced demyelination and spontaneous remyelination. *NeuroImage* **125**, 363–377 (2016).
47. Jelescu, I. O. *et al.* In vivo quantification of demyelination and recovery using compartment-specific diffusion MRI metrics validated by electron microscopy. *NeuroImage* **132**, 104–114 (2016).
48. Dong, J. W. *et al.* Diffusion MRI biomarkers of white matter microstructure vary nonmonotonically with increasing cerebral amyloid deposition. *Neurobiol. Aging* **89**, 118–128 (2020).
49. Tristão Pereira, C. *et al.* Synchronous nonmonotonic changes in functional connectivity and white matter integrity in a rat model of sporadic Alzheimer's disease. *NeuroImage* **225**, 117498 (2021).

50. Pavan, T. *et al.* Microstructure of White Matter, Probed With Diffusion MRI Modeling, Reveals Distinct Correlations Between Intra- vs Extra-Cellular Spaces and Tau Load. *Alzheimers Dement.* **19**, e078259 (2023).
51. Chung, S. *et al.* White Matter Tract Integrity: An Indicator of Axonal Pathology after Mild Traumatic Brain Injury. *J. Neurotrauma* **35**, 1015–1020 (2018).
52. Yung, A. R. *et al.* Mapping the onset of psychosis: the Comprehensive Assessment of At-Risk Mental States. *Aust. N. Z. J. Psychiatry* **39**, 964–971 (2005).
53. Tustison, N. J. *et al.* N4ITK: improved N3 bias correction. *IEEE Trans. Med. Imaging* **29**, 1310–1320 (2010).
54. Avants, B. B., Epstein, C. L., Grossman, M. & Gee, J. C. Symmetric diffeomorphic image registration with cross-correlation: evaluating automated labeling of elderly and neurodegenerative brain. *Med. Image Anal.* **12**, 26–41 (2008).
55. Ades-Aron, B. *et al.* Evaluation of the accuracy and precision of the diffusion parameter EStImation with Gibbs and NoisE removal pipeline. *NeuroImage* **183**, 532–543 (2018).
56. Veraart, J., Sijbers, J., Sunaert, S., Leemans, A. & Jeurissen, B. Weighted linear least squares estimation of diffusion MRI parameters: Strengths, limitations, and pitfalls. *NeuroImage* **81**, 335–346 (2013).
57. Mori, S., Wakana, S., Van Zijl, P. C. & Nagae-Poetscher, L. M. *MRI Atlas of Human White Matter*. (Elsevier, 2005).
58. American Psychiatric Association. *Diagnostic and Statistical Manual of Mental Disorders (4th Ed., Text Rev.).* (2000).
59. Kay, S. R., Fiszbein, A. & Opler, L. A. The Positive and Negative Syndrome Scale (PANSS) for Schizophrenia. *Schizophr. Bull.* **13**, 261–276 (1987).
60. Montgomery, S. A. & Asberg, M. A new depression scale designed to be sensitive to change. *Br. J. Psychiatry J. Ment. Sci.* **134**, 382–389 (1979).
61. Wallwork, R. S., Fortgang, R., Hashimoto, R., Weinberger, D. R. & Dickinson, D. Searching for a consensus five-factor model of the Positive and Negative Syndrome Scale for schizophrenia. *Schizophr. Res.* **137**, 246–250 (2012).
62. Fortin, J.-P. *et al.* Harmonization of multi-site diffusion tensor imaging data. *NeuroImage* **161**, 149–170 (2017).
63. Alemán-Gómez, Y. *et al.* Partial-volume modeling reveals reduced gray matter in specific thalamic nuclei early in the time course of psychosis and chronic schizophrenia. *Hum. Brain Mapp.* **41**, 4041–4061 (2020).
64. Brunner, E. & Munzel, U. The Nonparametric Behrens-Fisher Problem: Asymptotic Theory and a Small-Sample Approximation. *Biom. J.* **42**, 17–25 (2000).

65. Karch, J. D. Psychologists Should Use Brunner-Munzel's Instead of Mann-Whitney's U Test as the Default Nonparametric Procedure. *Adv. Methods Pract. Psychol. Sci.* **4**, 2515245921999602 (2021).
66. R Core Team. *R: A Language and Environment for Statistical Computing*. (R Foundation for Statistical Computing, Vienna, Austria, 2023).
67. Samartzis, L., Dima, D., Fusar-Poli, P. & Kyriakopoulos, M. White Matter Alterations in Early Stages of Schizophrenia: A Systematic Review of Diffusion Tensor Imaging Studies. *J. Neuroimaging* **24**, 101–110 (2014).
68. Peters, B. D. & Karlsgodt, K. H. White matter development in the early stages of psychosis. *Schizophr. Res.* **161**, 61–69 (2015).
69. Kochunov, P. & Hong, L. E. Neurodevelopmental and neurodegenerative models of schizophrenia: white matter at the center stage. *Schizophr. Bull.* **40**, 721–728 (2014).
70. Carletti, F. *et al.* Alterations in White Matter Evident Before the Onset of Psychosis. *Schizophr. Bull.* **38**, 1170–1179 (2012).
71. Cropley, V. L. *et al.* Accelerated Gray and White Matter Deterioration With Age in Schizophrenia. *Am. J. Psychiatry* **174**, 286–295 (2017).
72. Kraguljac, N. V., Guerreri, M., Strickland, M. J. & Zhang, H. Neurite Orientation Dispersion and Density Imaging in Psychiatric Disorders: A Systematic Literature Review and a Technical Note. *Biol. Psychiatry Glob. Open Sci.* **3**, 10–21 (2023).
73. Cheung, V. *et al.* Positive symptoms and white matter microstructure in never-medicated first episode schizophrenia. *Psychol. Med.* **41**, 1709–1719 (2011).
74. Kitamura, H. *et al.* Diffusion tensor analysis in chronic schizophrenia A preliminary study on a high–field (3.0T) system. *Eur. Arch. Psychiatry Clin. Neurosci.* **255**, 313–318 (2005).
75. Sato, Y. *et al.* Relationship Between White Matter Microstructure and Hallucination Severity in the Early Stages of Psychosis: A Diffusion Tensor Imaging Study. *Schizophr. Bull. Open* **2**, sgab015 (2021).
76. Pasternak, O., Kelly, S., Sydnor, V. J. & Shenton, M. E. Advances in microstructural diffusion neuroimaging for psychiatric disorders. *NeuroImage* **182**, 259–282 (2018).
77. Abdul-Rahman, M. F., Qiu, A. & Sim, K. Regionally Specific White Matter Disruptions of Fornix and Cingulum in Schizophrenia. *PLOS ONE* **6**, e18652 (2011).
78. Luck, D., Malla, A. K., Joober, R. & Lepage, M. Disrupted integrity of the fornix in first-episode schizophrenia. *Schizophr. Res.* **119**, 61–64 (2010).

79. Koshiyama, D. *et al.* Role of frontal white matter and corpus callosum on social function in schizophrenia. *Schizophr. Res.* **202**, 180–187 (2018).
80. Chen, S. *et al.* The role of white matter abnormality in the left anterior corona radiata: In relation to formal thought disorder in patients with schizophrenia. *Psychiatry Res.* **307**, 114302 (2022).
81. Meng, L. *et al.* Widespread white-matter microstructure integrity reduction in first-episode schizophrenia patients after acute antipsychotic treatment. *Schizophr. Res.* **204**, 238–244 (2019).
82. Ochi, R. *et al.* White matter microstructural organizations in patients with severe treatment-resistant schizophrenia: A diffusion tensor imaging study. *Prog. Neuropsychopharmacol. Biol. Psychiatry* **100**, 109871 (2020).
83. Elfaki, A. A. *et al.* STEREOLOGICAL EVALUATION OF BRAIN MAGNETIC RESONANCE IMAGES OF SCHIZOPHRENIC PATIENTS. *Image Anal. Stereol.* **32**, 145–153 (2013).
84. Kanaan, R. *et al.* White matter microstructure in schizophrenia: effects of disorder, duration and medication. *Br. J. Psychiatry* **194**, 236–242 (2009).
85. Wijtenburg, S. A. & Rowland, L. M. Chapter 19 - Schizophrenia spectrum disorders. in *Advances in Magnetic Resonance Technology and Applications* (eds. Laule, C. & Port, J. D.) vol. 9 469–487 (Academic Press, 2023).
86. Dunleavy, C., Elsworthy, R. J., Upthegrove, R., Wood, S. J. & Aldred, S. Inflammation in first-episode psychosis: The contribution of inflammatory biomarkers to the emergence of negative symptoms, a systematic review and meta-analysis. *Acta Psychiatr. Scand.* **146**, 6–20 (2022).
87. Goldsmith, D. R., Rapaport, M. H. & Miller, B. J. A meta-analysis of blood cytokine network alterations in psychiatric patients: comparisons between schizophrenia, bipolar disorder and depression. *Mol. Psychiatry* **21**, 1696–1709 (2016).
88. Marquand, A. *et al.* Conceptualizing mental disorders as deviations from normative functioning. *Mol. Psychiatry* **24**, (2019).
89. Zhuo, J. *et al.* Diffusion kurtosis as an in vivo imaging marker for reactive astrogliosis in traumatic brain injury. *NeuroImage* **59**, 467–477 (2012).
90. Budde, M. D. & Frank, J. A. Neurite beading is sufficient to decrease the apparent diffusion coefficient after ischemic stroke. *Proc. Natl. Acad. Sci.* **107**, 14472–14477 (2010).
91. Wang, Y. *et al.* Quantification of increased cellularity during inflammatory demyelination. *Brain* **134**, 3590–3601 (2011).

92. Falangola, M. F. *et al.* Histological correlation of diffusional kurtosis and white matter modeling metrics in cuprizone-induced corpus callosum demyelination. *NMR Biomed.* **27**, 948–957 (2014).

# Figure Legends

**Table 1**

Overview of the effect of various pathological processes on diffusion metrics, adapted from [44]. Astro- and microgliosis reduce water diffusivity and increase kurtosis via increased cellularity. Demyelination on the contrary translates to increased diffusivities and reduced kurtosis. When both are concomitant, they have competing effects. ↑: increase, ↓: decrease, ∼: unchanged. Metrics are defined in **Fig.1**.

**Figure 1**

Schematic of White Matter Tract integrity-Watson (WMTI-W) biophysical model. Axons are modeled as a collection of sticks embedded into an extra-axonal space. Estimated parameters are: axonal water fraction $f$, intra-axonal diffusivity, $D_a$, extra-axonal parallel and radial diffusivities, $D_{e,//}$ and $D_{e,\perp}$, and axonal orientation alignment, $c_2$. The latter is derived from the concentration parameter of the Watson distribution, κ and corresponds to $c_2 \equiv \langle cos^2\psi \rangle$, with $\psi$ being the angle between axons and the main bundle orientation. $c_2$ varies between ⅓, isotropic, and 1, perfectly parallel axons.

**Table 2**

Cohort demographics. HC amount to 135 Individuals, 79 HC were shared between HC-Y and HC-O. P-values refer to Wilcoxon's tests between clinical and HC groups. $\chi^2$ test is computed for the scanner and sex contingency table. Y: young, O: old, CPZ: chlorpromazine, Delay MRI-Clin. Ass.: difference in months between MRI scan and clinical assessment, SOFAS: Social and Occupational Functioning Assessment Scale, GAF: Global Assessment of Functioning, PANSS: Positive and Negative Syndrome Scale, MADRS: Montgomery-Asberg Depression Rating Scale.

**Figure 2**

Strip plot of the group comparisons. Each clinical group is compared to its respective HC group. *:p≤5e-2, **:p≤1e-2, ***:p≤1e-3, ****:p≤1e-4.

**Figure 3**

Heatmaps and brainplots of the JHU ROI group comparison. Top: group comparisons (y-axis right) heatmap of the Brunner-Munzel test significance levels for each dMRI metric (y-axis left) and each region of interest (x-axis). Bottom: brainplots of the same comparisons. The colorbar is shared. Red: clinical group > HC, Blue: clinical group < HC. NS: p>0.05, *:p≤5e-2, **:p≤1e-2, ***:p≤1e-3, ****:p≤1e-4.
*Abbreviations*: L: left; R: right; MIDCP: Middle cerebellar peduncle; PCT: Pontine crossing tract; GCC/BCC/SCC: Genu/Body/Splenium of corpus callosum; ; FX: Fornix (column and body); CST: Corticospinal tract; ML: Medial lemniscus; ICP/SCP: Inferior/Superior cerebellar peduncle; CP: Cerebral peduncle; ALIC/PLIC/RPIC: Anterior limb/Posterior Limb/ Retrolenticular part of internal capsule; ACR/SCR/PCR: Anterior/Superior/Posterior corona radiata; PTR: Posterior thalamic radiation; SAGSTR: Sagittal stratum; EC: External capsule; CING/CG: Cingulum (cingulate gyrus); CING/HIP: Cingulum (hippocampus); FX/STRIA: Fornix (crus) / Stria terminalis ; SLF: Superior longitudinal fasciculus; SFOF/IFOF: Superior/Inferior fronto-occipital fasciculus; IUF: Uncinate fasciculus; TPTM: Tapetum.

**Figure 4**

Hierarchical clustering of the correlation matrices between WM microstructure estimates and psychopathological symptoms domains. A: EP; B: SZ. Microstructure estimates were corrected for sex and quadratic age. The line diagrams indicate the clustering results. GAF: Global Assessment of Functioning scale; MADRS: Montgomery-Asberg Depression Rating Scale; Positive and Negative Syndrome Scales: pos.: positive; neg.: negative, dis.: disorganized; depr.: depressive; exc.: excited.

# Tables

**Table 1**

| Cellular process | Proposed changes in signal in DTI and DKI metrics | Validation experiments | Proposed changes in WMTI metrics | Validation experiments |
|---|---|---|---|---|
| Microgliosis | DTI ↓, DKI ↑ | Early stages of the mouse cuprizone intoxication[46] | $D_a$ ↓, $D_{e,//}$ ↓, $D_{e,\perp}$ ↓ | Early stages of the mouse cuprizone intoxication[46] |
| Astrogliosis | DTI ↓, DKI ↑ | Mouse traumatic brain injury model[89] | $D_a$ ↓, $D_{e,//}$ ↓, $D_{e,\perp}$ ↓ | Early stages of the mouse cuprizone intoxication[46] |
| Axonal swelling or beading | RD∼, MD↓, AD↓↓, RK∼, MK↑, AK↑↑ | Simulation in synthetic and electron microscopy-derived mouse substrates[104,105] | $D_a$ ↓ | Simulation of neurite beading[90] |
| Demyelination | RD↑↑, MD↑, AD∼, RK↓↓, MK↓, AK∼ | Cuprizone mouse model[46,47,91,92] | $f$ ↓, $D_{e,//}$ ↑, $D_{e,\perp}$ ↑ | Late stages of the mouse cuprizone intoxication[46,47,92] |
| Remyelination | RD↓↓, MD↓, AD∼, RK↑↑, MK↑, AK∼ | Cuprizone mouse model[46,47] | $f$ ↑, $D_{e,//}$ ↓, $D_{e,\perp}$ ↓ | Mouse cuprizone intoxication[47,*] |

*Opposite trends to demyelination were found for the metrics but were non-significant.

585 **Table 2**

| | | HC-Y (N=130) | | HC-O (N=84) | | EP (N=93) | | SZ (N=47) | | EP-(HC-Y) | SZ-(HC-O) | EP-SZ |
|---|---|---|---|---|---|---|---|---|---|---|---|---|
| | | Mean | SD | Mean | SD | Mean | SD | Mean | SD | p-value | p-value | p-value |
| Age (years) | | 26.8 | 6.8 | 31.9 | 8.1 | 24.7 | 5.5 | 38.1 | 9.4 | 3.0e-02* | 5.6e-05**** | p=3.5e-15**** |
| Age at Psychosis Onset (years) | | | | | | 23.0 | 5.8 | 23.8 | 9.3 | | | ns |
| Duration of illness (months) | | | | | | 16.3 | 15.5 | 160.8 | 77.9 | | | p=1.3e-18**** |
| CPZ-equivalent dose (mg/day) | | | | | | 341.0 | 274.5 | 319.6 | 287.7 | | | ns |
| Delay MRI-Clin. Ass. (months) | | 2.5 | 5.5 | 3.1 | 6.9 | 2.1 | 3.2 | 6.6 | 21.3 | | | p=1.0e-03** |
| PANSS: total | | | | | | 62.7 | 15.6 | 62.0 | 15.9 | | | ns |
| PANSS: positive | | | | | | 7.0 | 2.9 | 8.3 | 3.6 | | | p=2.3e-02* |
| PANSS: negative | | | | | | 14.9 | 5.7 | 14.0 | 5.4 | | | ns |
| PANSS: disorganized | | | | | | 5.7 | 2.2 | 6.5 | 2.2 | | | p=2.8e-02* |
| PANSS: excited | | | | | | 6.1 | 2.2 | 6.2 | 2.1 | | | ns |
| PANSS: depressed | | | | | | 8.2 | 2.8 | 8.1 | 3.3 | | | ns |
| GAF | | 83.9 | 4.4 | 83.4 | 4.7 | 56.2 | 11.2 | 56.0 | 13.2 | 1.6e-33**** | 4.6e-16**** | ns |
| MADRS tot. | | | | | | 12.5 | 8.4 | 13.2 | 8.6 | | | ns |
| | | N | Pct.% | N | Pct. | N | Pct.% | N | Pct.% | | | |
| Scanner | Prisma | 67 | 51.5 | 43 | 51.2 | 59 | 63.4 | 20 | 42.6 | $\chi^2$:6.3 | p=.096 ns | |
| | Trio | 63 | 48.5 | 41 | 48.8 | 34 | 36.6 | 27 | 57.4 | | | |
| Sex | Female | 46 | 35.4 | 35 | 41.7 | 26 | 28.0 | 13 | 27.7 | $\chi^2$:4.67 | p=.19 ns | |
| | Male | 84 | 64.6 | 49 | 58.3 | 67 | 72.0 | 34 | 72.3 | | | |

586

# Figures

**Figure 1**

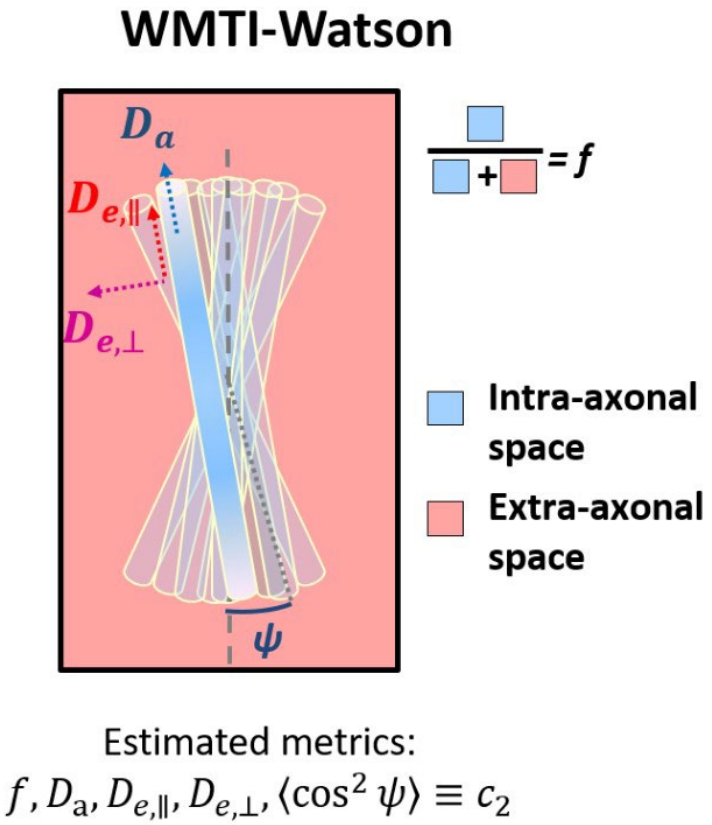

**Figure 2**

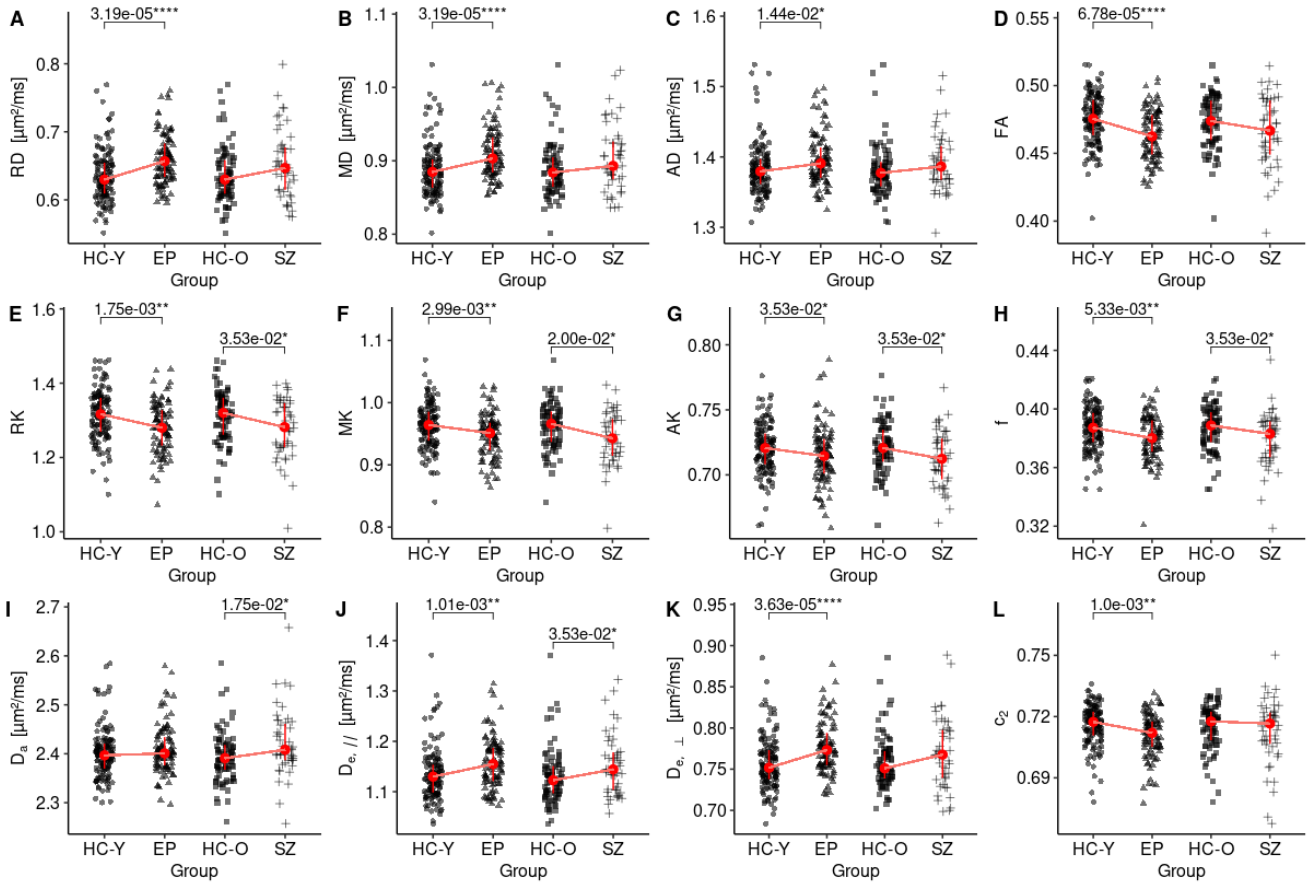
A
3.19e-05****
RD [μm²/ms]
B
3.19e-05****
MD [μm²/ms]
C
1.44e-02*
AD [μm²/ms]
D
6.78e-05****
FA
E
1.75e-03**
3.53e-02*
RK
F
2.99e-03**
2.00e-02*
MK
G
3.53e-02*
3.53e-02*
AK
H
5.33e-03**
3.53e-02*
f
I
1.75e-02*
D_a [μm²/ms]
J
1.01e-03**
3.53e-02*
D_e, // [μm²/ms]
K
3.63e-05****
D_e, ⊥ [μm²/ms]
L
1.0e-03**
c_2
HC-Y
EP
HC-O
SZ
Group

**Figure 3**

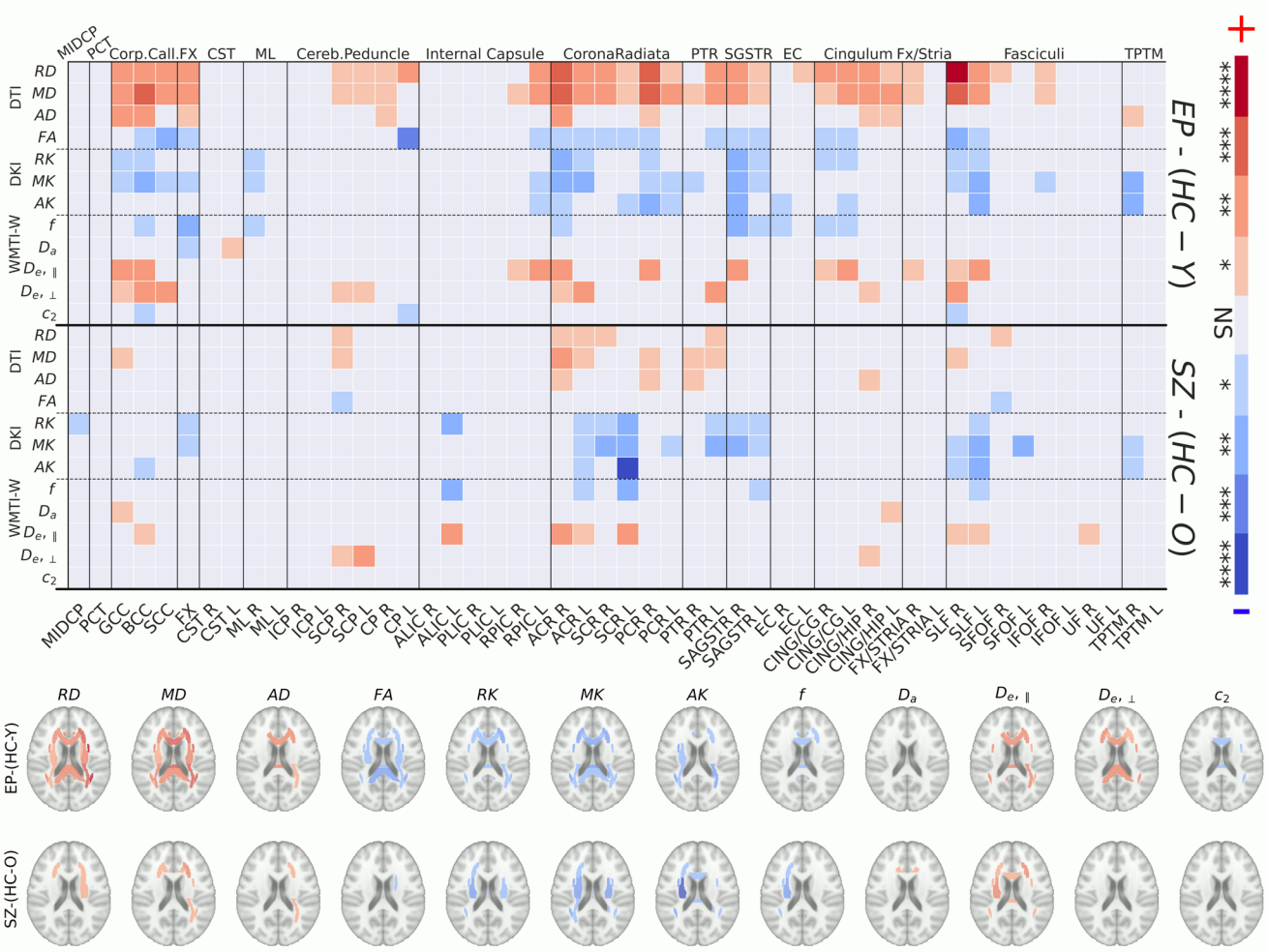
MIDCP
PCT
Corp.Call.FX
CST
ML
Cereb.Peduncle
Internal Capsule
CoronaRadiata
PTR
SGSTR
EC
Cingulum Fx/Stria
Fasciculi
TPTM
DTI
DKI
WMTI-W
RD
MD
AD
FA
RK
MK
AK
f
$D_a$
$D_{e,\parallel}$
$D_{e,\perp}$
$c_2$
EP - (HC − Y)
SZ - (HC − O)
+
−
NS
*
**
***
****
MIDCP
PCT
GCC
BCC
SCC
FX
CST R
CST L
ML R
ML L
ICP R
ICP L
SCP R
SCP L
CP R
CP L
ALIC R
ALIC L
PLIC R
PLIC L
RPIC R
RPIC L
ACR R
ACR L
SCR R
SCR L
PCR R
PCR L
PTR R
PTR L
SAGSTR R
SAGSTR L
EC R
EC L
CING/CG R
CING/CG L
CING/HIP R
CING/HIP L
FX/STRIA R
FX/STRIA L
SLF R
SLF L
SFOF R
SFOF L
IFOF R
IFOF L
UF R
UF L
TPTM R
TPTM L
EP-(HC-Y)
SZ-(HC-O)

596 **Figure 4**

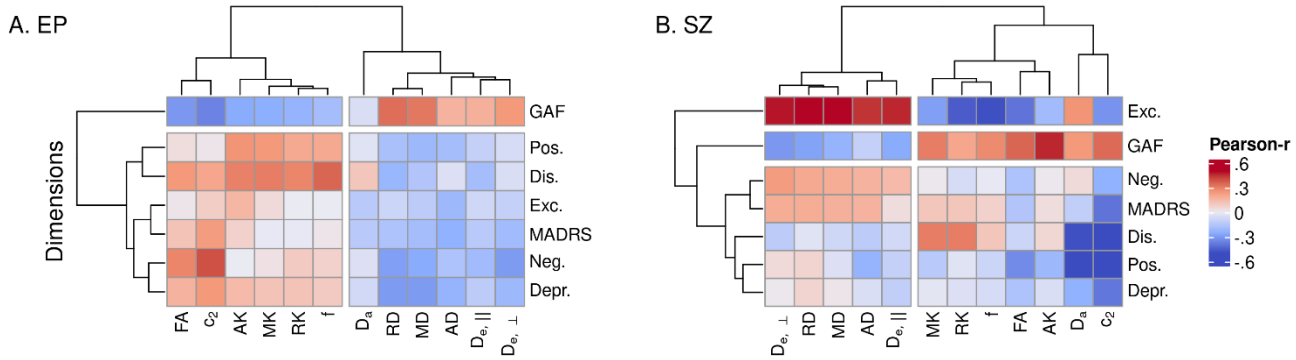


597